



Surface modification of mild steel using a combination of laser and electrochemical processes



Alistair Speidel^a, Adrian Hugh Alexander Lutey^b, Jonathon Mitchell-Smith^a, Graham A. Rance^c, Erica Liverani^b, Alessandro Ascari^b, Alessandro Fortunato^b, Adam Clare^{a,*}

^a Advanced Component Engineering Laboratory (ACEL), University of Nottingham, University Park, Nottingham NG7 2RD, United Kingdom

^b Dipartimento di Ingegneria Industriale (DIN), Università di Bologna, Viale Risorgimento 2, Bologna 40136, Italy

^c Nanoscale and Microscale Research Centre, University of Nottingham, University Park, Nottingham NG2 7RD, United Kingdom

ARTICLE INFO

Article history:

Received 22 July 2016

Revised 28 September 2016

Accepted in revised form 29 September 2016

Available online 30 September 2016

Keywords:

Surface texturing

ECM

EJM

Hybrid processing

Laser processing

ABSTRACT

Traditional methods for achieving hierarchical surface structures include highly specified, deterministic approaches to create features to meet design intention. In this study microstructural alteration was undertaken using laser apparatus and secondary texturing was achieved *via* succeeding electrochemical processes. Electrochemical jet machining (EJM) was performed on mild steel subjected to laser pre-treatment using power densities of 4167 and 5556 W/cm² with pulse durations from 0.3–1.5 s. Results show that in combination, laser pre-treatment and EJM can alter the exposed surface textures and chemistries. Here, machined surface roughness (*S_a*) was shown to increase from approximately 0.45 μm for untreated surfaces to approximately 18 μm for surfaces subjected to extreme laser pre-treatments. After pre-treatments materials were characterised to appraise microstructural changes, shown to be martensite formation, reinforced by complementary simulation data, and significant increases in observable hardness from approximately 261 HV for the as-received material to over 700 HV after pre-treatment. The greater hardness was retained after EJM. Exposed martensitic lath structures at machined surfaces are shown to be partially responsible for surface roughness increases. The surfaces were explored with energy dispersive X-ray spectroscopy (EDS) and Raman spectroscopy demonstrating changes in apparent surface chemistry. This analysis revealed increasing oxide formation at the surface of the pre-treated EJM surface, a further contributory factor to surface roughness increases. This new process chain will be of interest to manufacturers seeking to control surface morphology for applications including micro-injection mould/die manufacture. While demonstrated here for steel similar mechanisms are exploitable in other material systems. A new technique has been demonstrated, resulting from the models and processes presented to couple laser and electrolyte jet processing for complex surface preparation.

© 2016 The Authors. Published by Elsevier B.V. This is an open access article under the CC BY license (<http://creativecommons.org/licenses/by/4.0/>).

1. Introduction

Unlike conventional shear based machining processes, electrochemical machining (ECM) removes material through the process of anodic dissolution. ECM methods are attractive to manufacturers since no residual stress is created at the machined surface and therefore the material properties and the microstructure are unaffected [1]. Invoking location specific microstructural changes, then exposing them through selective anodic dissolution can therefore be used to create an alternative topography closely related to the underlying microstructure.

Electrochemical jet machining (EJM) is an ECM technique whereby electrolyte is expelled through a nozzle (cathode) as a column and impinging upon a workpiece (anode) causing localised anodic dissolution [2]. Unlike more established ECM techniques EJM does not require

expensive tooling and complex geometries can be realised without the need for masking. Localised material removal rates are also enhanced by the higher current densities achievable through the well-defined electrolyte column [3]. The alteration of EJM parameters alone has already been shown to create a wide range of observable surface textures [4,5], however, when used in conjunction with a hardening pre-treatment process, this variety of surface textures could be applied to create more mechanically robust surfaces.

A schematic of a typical EJM arrangement is shown in Fig. 1. A potential difference is applied across the workpiece and the nozzle. Material removal occurs directly below the nozzle and follows a Gaussian type current density distribution reflected in the cut profile [6]. The hydraulic jump phenomenon and the resulting thin radial film surrounding the impingement area serves to restrict the current density field and therefore material removal to directly below the electrolyte jet [7], therefore the electrolyte velocity in the EJM process must be great enough to cause the phenomenon [8]. Further enhancement of machining

* Corresponding author.

E-mail address: adam.clare@nottingham.ac.uk (A. Clare).

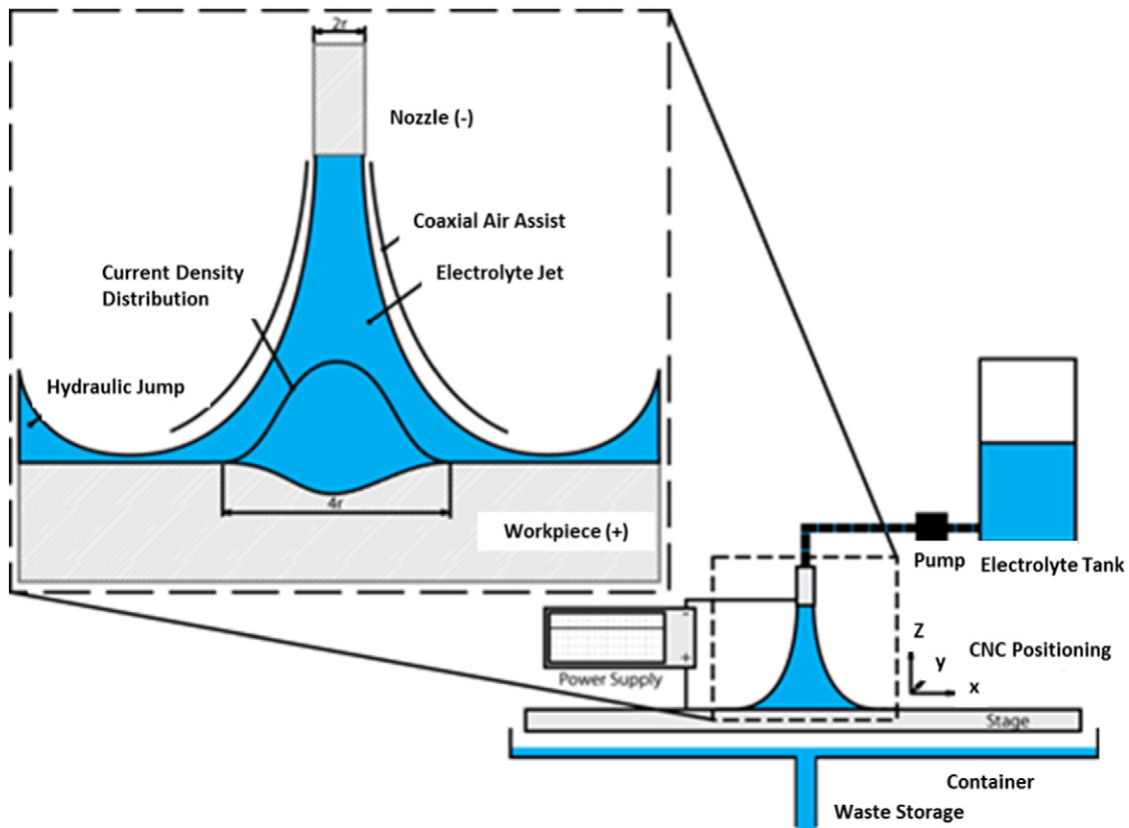


Fig. 1. Schematic of a typical EJM arrangement as that used in this study.

precision is achieved through the application of an air shroud which acts to constrict the jet further decreasing the machined area [9]. Current is applied using a DC power supply and fresh electrolyte is fed to the nozzle from a storage tank using a gear pump system.

Laser surface treatment is a well-established method for invoking localised microstructural changes *via* laser heating of a surface layer and subsequent quenching due to thermal conduction into the work piece [10]. This process is often employed as a substitute for induction hardening with advantages in terms of flexibility, ease of implementation and more localised application. Hardened layer depth is typically in the order of 0.05–1 mm where surface melting is to be avoided. The necessary laser power is a function of the focused beam spot size, scanning speed, target material composition (determining thermal and absorption response) and surface roughness. At low to moderate laser fluence, residual stresses are compressive leading to improved fatigue life, a characteristic that is potentially of great importance for highly stressed textured surfaces where shot peening is presently employed to improve fatigue life [11]. Local microstructural modification using laser processes is now feasible in most manufacturing settings with predictable results as a consequence of significant research, which used in this study [12,13,14].

It is possible to use pulsed laser processing to control surface roughness at different scales, and pico- and femtosecond regime laser machining processes also allow for high resolution deterministic surface creation [15,16]. Material response is known to be a function of thermal and mechanical properties however, these processes do not allow for the exposure of the preinstalled microstructural features. Also, since ablation is rapid the hardening profile is distinct from continuous wave laser surface treatment. Furthermore, the capital cost of these systems is an order of magnitude higher than the cost for the simple apparatus used in this study.

Low cost generation of controlled surface textures remains a challenge for manufacturers. Generation of deterministic surfaces requires

repeatable and precise control of the process. Limitations for these techniques usually relate to the precision of the translation apparatus and the smallest interaction volume that can be affected. The latter is characteristic of the process physics. In an attempt to create equally functional but stochastic surfaces this study investigates controlling and exploiting material microstructures for complex surface creation on the microscale. Herein, material pre-treatments have been investigated to alter the surface topography and resulting roughness of an EJM processed surface, while retaining pre-treatment induced hardening. Laser pre-treatments of steels can be used to modify the response of the materials to the electrochemical jet process for the purpose of creating variable microstructure, hardened surfaces for industrial applications. Characterisation of the resulting surfaces has been undertaken to assess the phases present at the exposed surfaces illustrating different chemical effects dependent on both the laser and EJM parameters used in the study. The findings of this study could have potential applications in fields where performance characteristics, topological differences, and increases in material hardness across the same component at the microscale are desired, such as micro-injection moulds where robust micro-textured surfaces that are highly resistant to wear are desired [17]. To this end, the material hardness was appraised after pre-treatment and subsequent electrochemical processing. Microscale surface texture control by EJM has also been explored to control surface super-hydrophobicity [18].

2. Experimental

2.1. Material type

39NiCrMo3 steel, of the composition given in Table 1, was considered in this study due to its widespread use in general engineering applications as a result of its excellent compromise between cost, mechanical characteristics, machinability and well understood heat

Table 1
39NiCrMo3 nominal composition, all values in wt%.

C	Si	Mn	Ni	P	S	Cr	Mo
0.35–0.43	0.15–0.4	0.5–0.8	0.7–1	Max 0.035	Max 0.035	0.6–1	0.15–0.25

treatment schedule. The material has good hardenability, strength and toughness, finding applications in stressed components such as shafts and gears across all mechanical engineering disciplines. Samples of 10 × 10 × 10 mm were employed for all experiments.

2.2. Laser setup, simulations and EJM system

A diode laser of maximum power output of 3.3 kW and a wavelength of 930 nm was utilised for all laser exposures. The laser system used was equipped with a 150 mm focal length focusing lens achieving a 6 × 6 mm square top-hat intensity distribution. Stationary laser exposures were performed on the 39NiCrMo3 samples with ten different laser power/dwell time combinations, the details of which are given in Table 2. In all cases, laser focus was at the centre of the exposed sample face to avoid boundary heating and thermal saturation effects. A numerical simulation was used to predict maximum surface temperatures and cooling rates for all laser exposures. Complete descriptions of the model, numerical method and temperature-dependent material properties have been presented in previous work [19]. The model is based on Fourier's equation with temperature dependent material properties according to Eq. (1).

$$\rho C_p \frac{\delta T}{\delta t} + Q = \nabla(k\nabla T) \tag{1}$$

where ρ is the workpiece density (g/m³), Cp the specific heat capacity at constant pressure (J/gK), T the temperature (°K), Q the absorbed energy density (W/m³) and k the thermal conductivity (W/mK). The simulation domain was the same size as the tested samples (10 × 10 × 10 mm), with the incident laser beam acting as a boundary heat source according to the optical absorption of the sample and a 6 × 6 mm Gaussian top hat laser intensity distribution. The domain was divided into elements of size 200 μm and resolved numerically. Though the fidelity of the simulation has previously been verified for surface temperatures up to the melting point (1540 °C), the fidelity at higher temperatures was expected to be limited as a consequence of the lack of material data concerning radiant heat loss and evaporation phenomena. Nonetheless, the calculation was expected to give a reasonable indication of cooling rates to verify the microstructural observations. Typically in large area laser processing, the spot is rastered over a surface in adjacent tracks. Track overlap has been shown to create multiple distinct microstructural regions. However, previous laser surface treatment work has shown that process control can be used to ensure uniform properties even in overlap regions [20].

Table 2
Details of the range of laser treatments and accompanying simulation results used within this study.

Laser power (W)	Pulse duration (s)	Energy passed (J)	Max. temp. (°C, simulated)	Cooling rate at A _{R3} point, 790 °C (K°C/s, simulated)	Time A _{R3} → M _s , (790 → 330 °C) (s, simulated)
1500	0.25	375	1027	6.35	0.216
1500	0.3	450	1119	3.80	0.264
2000	0.38	760	1662	1.83	0.456
2000	0.5	1000	1834	1.40	0.624
2000	0.63	1260	1988	1.13	0.840
2000	0.75	1500	2112	0.94	1.096
2000	0.88	1760	2237	0.79	1.448
2000	1	2000	2334	0.66	1.896
2000	1.5	3000	2650	0.39	>2

A simulated temperature–time graph at the centre of the laser interaction zone for each of the treatments is shown in Fig. 2 and values for the simulated cooling rates at 790 °C, the A_{R3} point (the temperature during cooling, at which the transformation from austenite to ferrite starts) for 39NiCrMo3, are given in Table 2. For this steel, the martensite start temperature, M_s, is approximately 330 °C and the simulations show the A_{R3} → M_s time to be no >2 s predicting the occurrence of the diffusionless transformation from austenite to martensite for all trials.

Laser pre-treated specimens were then subject to EJM. The process used in this study was carried out at a fixed current and floating voltage. The electrochemical treatment was kept constant throughout the trials. A three axis (X, Y, Z) precision NC EJM platform was used in this study where tool paths and all control parameters are pre-programmed (Table 3). Electrolyte is supplied to the nozzle using a gear pump system and the resulting waste is gravity drained from the workpiece and collected in storage tanks below the EJM rig for subsequent disposal. Further details of the platform can be found in earlier work [21].

2.3. Characterisation techniques

In this study, the processed surfaces were analysed using an Alicona InfiniteFocus G5 and the resulting 3D areal surface data were characterised in terms surface texture through analysis of roughness (Sa) using MountainsMap Premium 7.1 software under ISO 25178. Electron micrographs were acquired using both FEI XL30 and Hitachi-S2600 N SEM instruments. Full colour optical micrographs of the material microstructure were acquired after the etching of a polished specimen piece (nital, 2%) using a Nikon Eclipse LV100ND microscope (at ×20 and ×50 magnification) and subsequent microstructural measurements were undertaken using ImageJ software. Hardness (HV) was appraised using a Buehler Vickers hardness tester. Chemical compositions (wt% and at%) were analysed using an Oxford Instruments X-Max 80 SDD EDS system at constant detection times (60 s), beam parameters and sampling areas (20 kV primary beam, 3000 μm², ×5200 magnification) before processing using proprietary Inca software. Surface oxide phases present after EJM were analysed using Raman vibrational spectroscopy. Raman vibrational spectra were recorded on a Horiba–Jobin–Yvon LabRAM HR Raman microscope, with an excitation laser wavelength of 532 nm (power = ~16 mW) and a 600 lines/mm grating using a Synapse CCD detector. The Raman shift was calibrated using the Rayleigh line and a Si(100) reference sample. A typical spectrum was acquired in 30–60 s, with 8 accumulations to reduce the signal to noise ratio. Raman spectroscopic line-maps were generated using the relative intensities of known vibrational modes attributable to haematite, (A_{1g} and E_{2g}, 180–330 cm⁻¹), and magnetite (A_{1g}, 600–750 cm⁻¹).

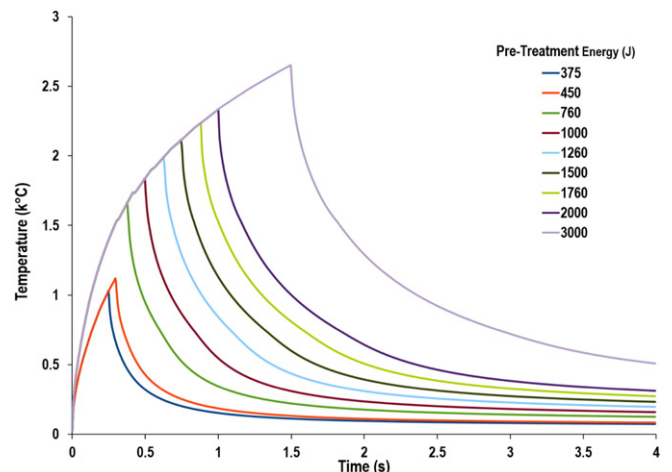


Fig. 2. Simulated heating and cooling (°C/s) curves for each pre-treatment.

Table 3
EJM parameters used in this study.

Machining parameter	Value
Current density, J (A/cm ²)	400
Electrolyte (NaNO ₃ , aq) concentration (M)	2
Nozzle internal diameter (μm)	250
Standoff distance (mm)	0.5
Feed rate (μm/s)	100
Flow rate (mL/min)	60

Spectral acquisitions were taken at 5 μm intervals along horizontal lines 130–180 μm in length across the non-machined surface, track edge, and track base.

2.4. Sample preparation

Sample preparation was undertaken according to Fig. 3. The as-received material, supplied in the solution annealed condition, was ground and polished to a mirror finish using diamond grit (1 μm) before being subjected to a defined laser treatment (Table 2) and subsequently subjected to a discrete electrochemical treatment using EJM apparatus (Table 3). Laser processing of the samples led to marked thermally induced oxidation of the steel. The oxide layers that were formed in the laser treatment process appeared to be highly resistive and thus inhibited the anodic dissolution of the underlying substrate material. This layer was mechanically removed by polishing as the focus of this study was to investigate the effect of microstructure on response to EJM. In this work, pre-treatments were undertaken in air and as such, this processing step could be eliminated though processing in an inert atmosphere. The resulting EJM tracks were then characterised with specific interest taken in the comparison between the interaction zones where the material was affected by both the laser and the electrochemical process and the zones where the material was affected only by the electrochemical treatment.

As a material removal process, EJM removes the workpiece surface to a depth dependent on the key process parameters of current density, dwell and electrochemical equivalence of the substrate [22]. In this study, it is important that the depth of the laser-treated zone must extend deeper into the specimen than the expected depth of the electrochemical machining process in order to confidently appraise impacts of the laser-induced microstructural changes. The depth of the heat

affect zone, (HAZ), is intrinsically linked to energy input in the laser processing step and has been both simulated and experimentally confirmed for all of the laser pre-treatments as shown in Fig. 4. The machining depth at the parameters used in the EJM process was understood to be fewer than 100 μm for this material type. This is less than the experimentally observed HAZ depth for all laser pre-treatments used within this study, thus there was no risk of machining completely through the HAZ to reveal a surface characteristic of the bulk specimen and not the laser treatment. In addition cross sectional micrographs indicate homogeneity in the microstructure of the region machined via EJM.

3. Results

3.1. Microstructural characterisation and hardness testing

Specimens of each laser treatment were sectioned, polished and etched to assess the effects of the laser treatment on the microstructure. Prior simulations demonstrated that a significant amount of martensite should have been present in the samples after laser treatment. This was confirmed by optical microscopy, which showed a marked difference in the microstructure dominated by lath martensite, compared with the ferritic microstructure of the as-received material. The optical micrographs in Fig. 5 clearly illustrate the expected martensitic microstructure for both high and low energy pre-treatments. The hardness of specimens was tested for all trials before laser treatment, after laser treatment and after electrochemical processing. In all cases the hardness at the surface of the samples was increased as a result of the formation of martensite in the pre-treatment. The graph in Fig. 5c illustrates this hardening effect where the as-received material shows a hardness of approximately 261 HV (red). After pre-treatment, this is shown to increase to over 700 HV for most of the trials (blue series), and this hardening effect is somewhat retained after electrochemical processing (purple series). The hardness of the electrochemically machined pre-treated surfaces is greater than the as-received material hardness in all cases tested here, and appear to be significantly harder than the non-pre-treated electrochemically machined surfaces (green).

The exposed surface of the track after the electrochemical treatment was observed using SEM in order to visualise changes to the surface texture caused by the pre-treatment. Fig. 6 shows a marked difference between the resulting surfaces of the EJM-laser interaction zone and the

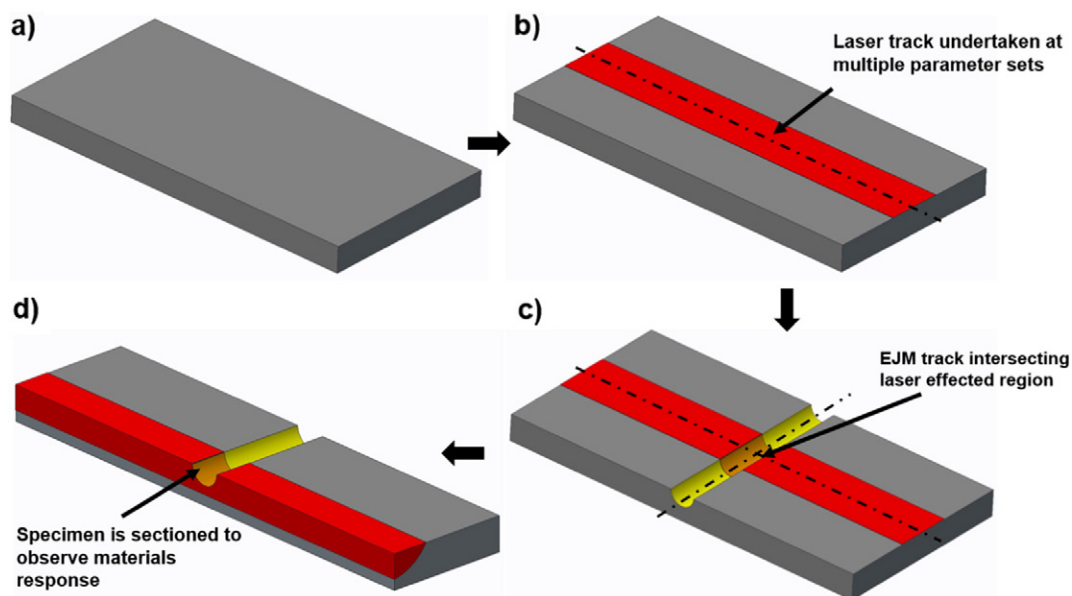


Fig. 3. Process steps: a) polished material, b) laser processing (red track), c) electrolyte jet machining (yellow track) showing interaction zone (orange region), d) cross-sectioned laser track.

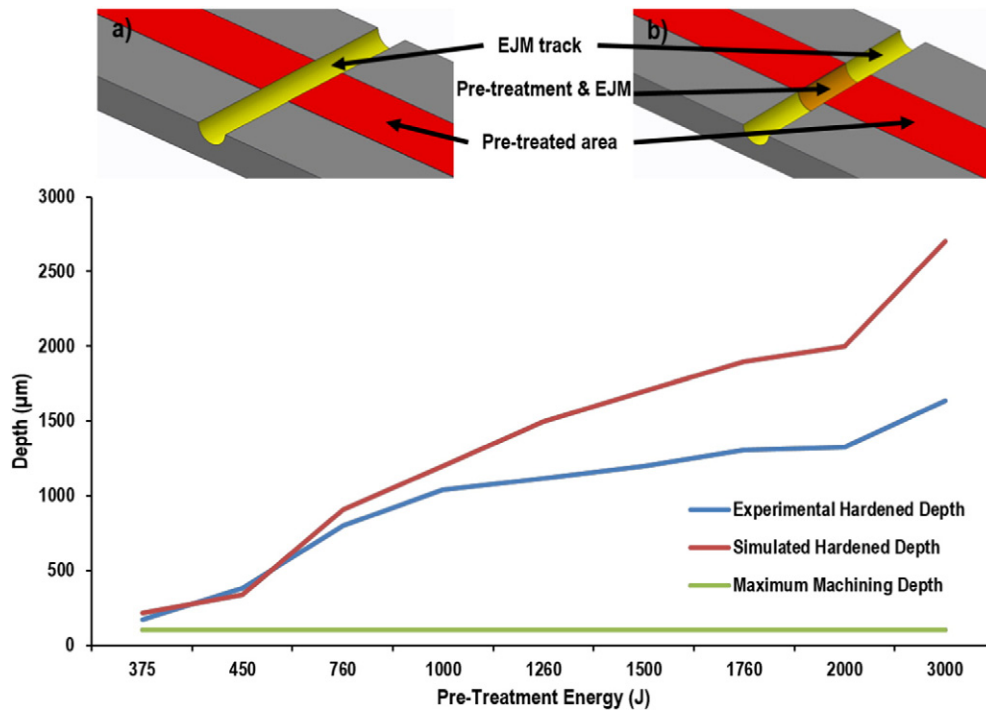


Fig. 4. Graph showing experimental and simulated (blue and red, respectively) hardened depths compared with the maximum machined depth of the EJM track (green). Inset a) undesirable case resulting from complete penetration of pre-treated zone, inset b) desirable case and generation of laser and EJM modified zone.

EJM-only zone (orange and yellow regions, respectively see Fig. 2) of the sample subjected to pre-treatment of 1260 J. The exposed surface in the laser-EJM interaction zone is defined by relatively large plate-like structures with lengths ranging from 3 to 10 μm and thicknesses of $<1 \mu\text{m}$. The absence of such plate like features in the untreated surfaces indicates that the microscale topography post-machining is closely related to the effects of the pre-treatment, and therefore it follows that the observable plate-like features in the laser processed surface are martensitic laths.

Although direct quantitative analysis of lighter elements such as carbon is not generally possible using EDS, trends may be drawn which can be used to determine changes in the material response to the electrochemical treatment caused by the laser pre-treatment. Fig. 7a shows lower apparent surface carbon concentrations in the electrochemically machined areas after laser pre-treatment compared with the EJM only areas for all trials undertaken. It is proposed that the laser-induced material changes, such as decarburisation, are responsible for the decrease in the apparent surface carbon in the electrochemically machined surfaces after pre-treatment. The maximum temperature in each pre-treatment case was predicted to be over 1000 $^{\circ}\text{C}$ and decarburisation is understood to occur well below these temperatures during thermal treatments outside of an inert atmosphere [23].

In Fig. 7b, oxygen signal at the electrochemically machined surface is shown to increase when the total energy input of the laser pre-treatment is $>1000 \text{ J}$. Pre-treatments of higher energy than 760 J lead to temperatures above 1540 $^{\circ}\text{C}$ (the melting point of this steel), therefore oxygen diffusion from the atmosphere into the bulk material upon laser pre-treatment is postulated to be responsible for this effect. Oxygen diffusion into the laser treated material is supported by evidence in Fig. 7a indicating laser-induced decarburisation in this mild steel.

3.2. Surface roughness

In this study, the roughness of the exposed surface (S_a) after the electrochemical treatment was shown to increase with pre-treatment

energy shown in Fig. 8. This has been observed for pre-treatments $>450 \text{ J}$. Therefore the change in surface texture has been linked to the laser-induced alteration of the internal microstructure. In 39NiCrMo3, all of the pre-treatment conditions trialled resulted in cooling rates sufficiently fast to lead to martensite formation. Martensitic lath revealed by the subsequent electrochemical processing is illustrated in Fig. 8 inset b), which also shows the resulting plate-type features at the surface contributing to the observed increase in roughness (S_a). Pre-treatments of 450 J and below were shown to result in negligible surface texture change in comparison to EJM surfaces having undergone no prior laser treatment, although martensite was still formed as a major phase in the pre-treatment.

Significant increases in roughness are demonstrated for pre-treatments $>760 \text{ J}$, and appear to increase with machined-surface oxygen signal (Fig. 7). The implication is that a contribution to the increased roughness is caused by increased levels of surface oxides after the electrochemically machining step. In this study pre-treatments of fewer than 760 J did not result in workpiece melting and therefore thermally dependent effects, such as diffusion, would have been less pronounced. High levels of oxygen diffusion into the bulk material at higher energy pre-treatments may have led to higher levels of surface oxides after the ECM process, thus making a partial contribution to the different surface texture.

3.3. Raman spectroscopy analysis

Inspection by EDS showed significant oxygen at the machined surface all of the samples, appearing to increase with pre-treatment energies of $>1000 \text{ J}$. Raman spectroscopy was subsequently undertaken to characterise the chemistry of the exposed surface after machining. The Raman vibrational spectra for common iron oxides and oxyhydroxides have been well reported, and compared with the results from this study [24].

Post-EJM the major oxide constituent of the resulting track bases and edges closest to the base is shown to be haematite, $\alpha\text{-Fe}_2\text{O}_3$,

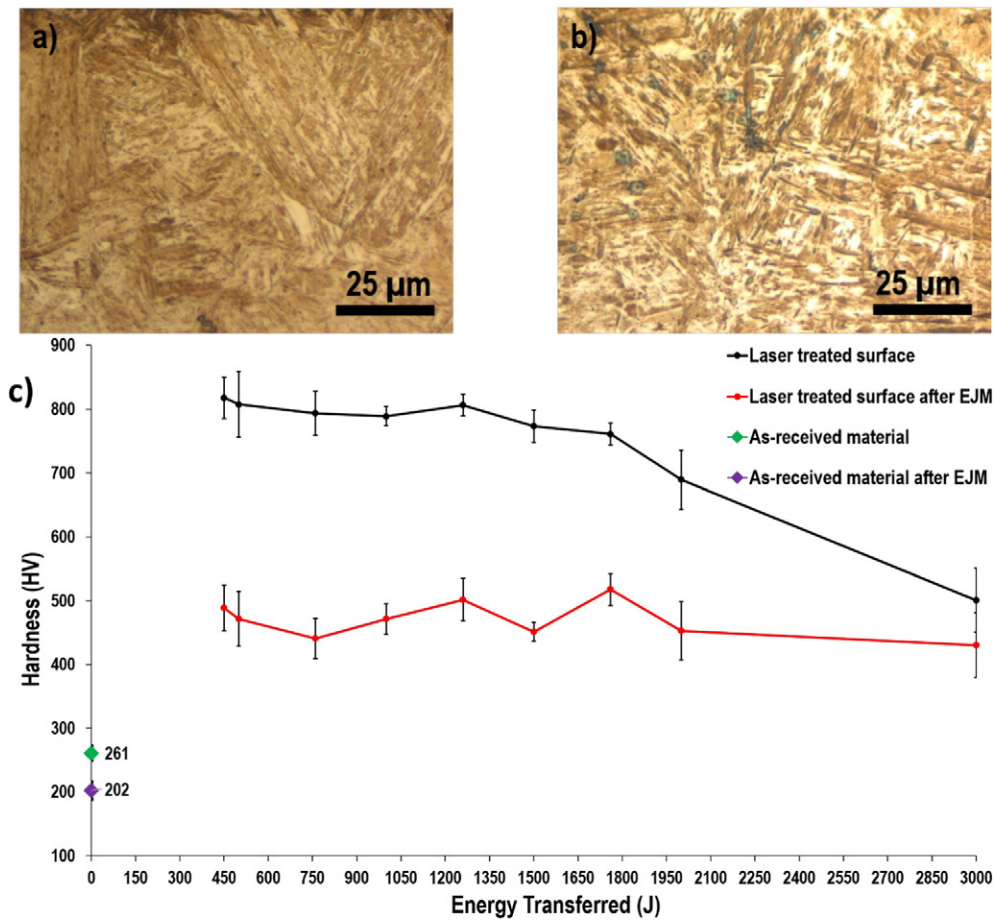


Fig. 5. Martensitic microstructure of HAZ. Optical micrographs of: a), low energy pre-treatment of 760 J; b), high energy pre-treatment of 3000 J. c) graph of measured hardness of as-received material before (red), and after EJM (green). This is compared with material hardness after each of the pre-treatments (blue series), and after subsequent EJM treatments (purple series).

shown in Fig. 9. The high intensity bands located at 200–280 cm^{-1} correlate well with known Fe–O stretching vibrations of A_{1g} and E_{2g} symmetry in haematite [25]. The broad but intense band situated at approximately 1300 cm^{-1} matches well with the two-magnon scattering resulting from the antiferromagnetic nature of haematite [26]. The assignment of bands attributable to maghemite, $\gamma\text{-Fe}_2\text{O}_3$, is challenging however as the primary bands overlap with those of magnetite, Fe_3O_4 . Maghemite has previously been reported in classical electrochemical studies to compose the majority of the exposed passivating layer in

iron [27]. The Raman spectra show a sharp vibrational mode at 668 cm^{-1} in the machining regions of lower current density (Fig. 9), which correlates well with known Fe–O vibrations of A_{1g} symmetry in magnetite [24]. Magnetite has been shown to make up the inner layer of the oxide film and occurs as a product of one of the first steps of the anodic dissolution process [28]. That magnetite can be observed in areas of lower current density suggests that the anodic dissolution reaction has not proceeded to the further oxidation product, Fe_2O_3 , an effect which is proposed to be the result of the lower total charge passed

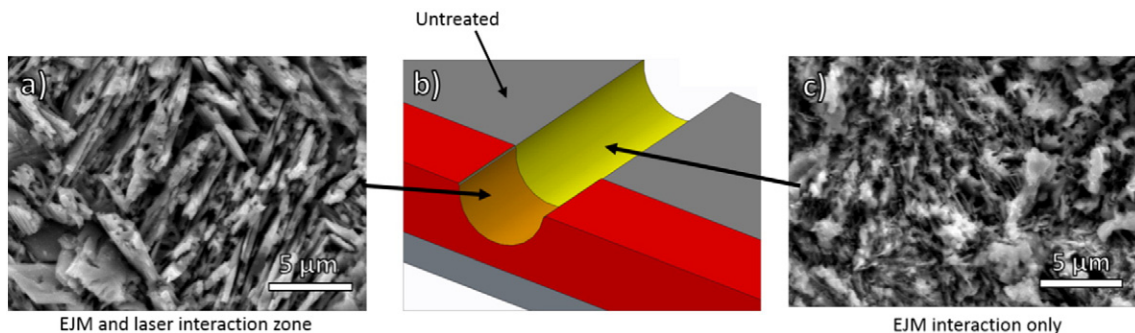


Fig. 6. a) exposed surface of laser-EJM interaction zone, b) figure of sectioned track, c) exposed surface after EJM in the non-laser treated zone.

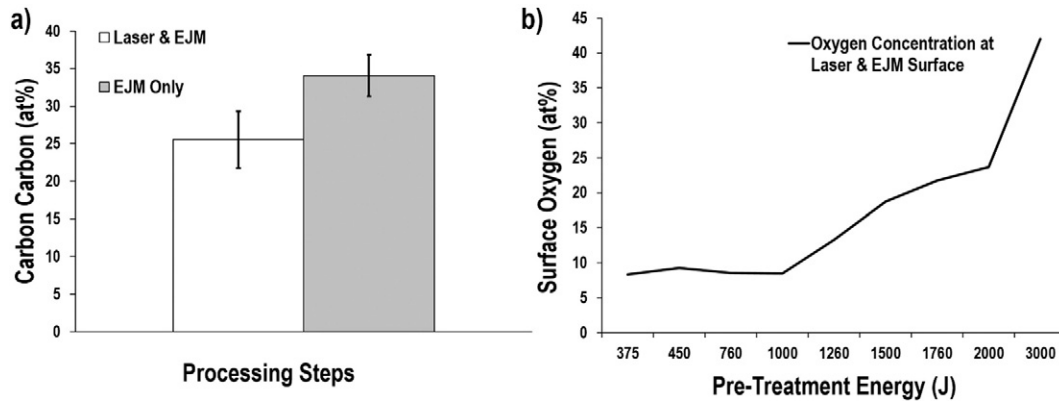


Fig. 7. a) Carbon concentration (at%) at the machined surface showing the general disparity between laser and EJM interaction zone and EJM only zones. b) Oxygen concentration (at%) at the machined surface showing an increase in surface oxygen with laser treatment.

in the edge regions. It should be noted that the polished, unprocessed surfaces show a lack of oxide vibrational modes demonstrating that the iron oxides observed are formed as part of, or as a consequence of, the EJM process. The recorded spectra appeared to show little difference between iron oxides present at the exposed track surfaces between specimens with and without laser pre-treatment. Conversely, track surfaces in areas that were not pre-treated often showed the existence of a broad band situated at approximately $1550\text{--}1650\text{ cm}^{-1}$ which corresponds well to the C—C stretching vibration of E_{2g} symmetry (G band) in graphitic carbon [29]. The associated graphitic stretching vibration of A_{1g} symmetry (D band) would be masked by the two-magnon scattering of haematite, therefore no comment can be made regarding the purity of the graphitic phase which occurred outside of the pre-treated area. Graphitic carbon was not observable in the pre-treated surfaces of the same sample pieces implying that thermal phenomena such as decarburisation could have been responsible for the apparent depletion.

4. Discussion

4.1. Surface roughness and hardness

The increase in surface roughness due to laser pre-treatment has been linked in this study to a laser-induced change in the starting material. The formation of lath martensite has been observed to affect the microscale structure of the machined surface and the influence on the surface roughness (S_a) has been measured. The observation of plate features during SEM is proposed to occur *via* the revelation of martensitic lath from the surface of the material as a consequence of the electrochemical treatment; the mechanism illustrated in Fig. 10. The exposure of martensite from the bulk of the material therefore represents a significant contributory factor to the increased roughness with laser pre-treatment. It is proposed that similar mechanisms may be exploited for the processing of other material systems. The formation of martensite in the pre-treatment process also significantly increases the hardness

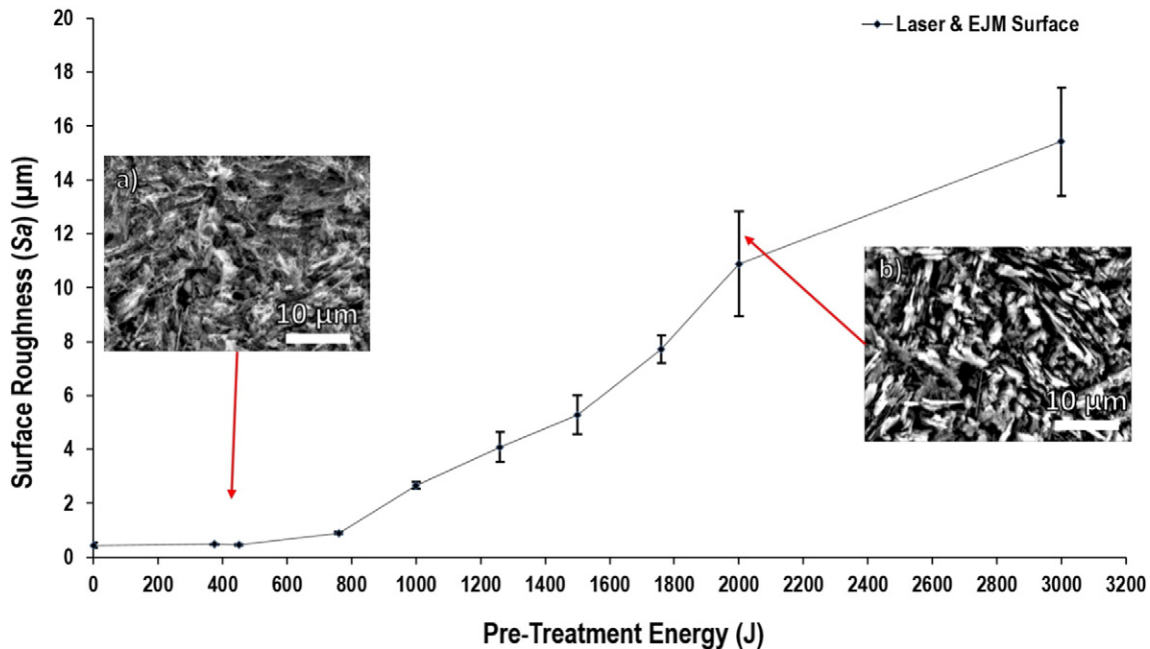


Fig. 8. Surface roughness (S_a) of EJM track bases at different pre-treatments; inset a) SEM micrograph of EJM surface after pre-treatment of 450 J and inset b) SEM micrograph of EJM surface after pre-treatment of 2000 J, showing the change in texture of the exposed surface resulting in the differences in roughness.

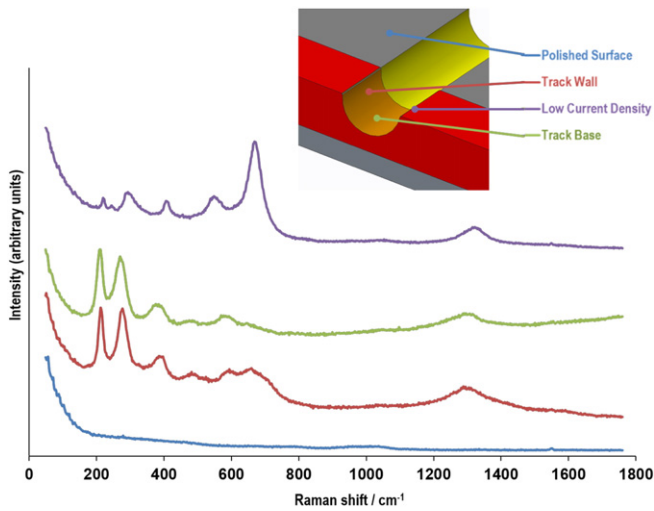


Fig. 9. Typical Raman spectra acquired from mild steel: a) polished surface (blue), b) track wall EJM-laser interaction zone (red), c) track base EJM-laser interaction zone (green) d) current density zone (purple), inset, simulated view of specimen piece showing areas of spectral acquisition.

of the material. This effect is shown in the graph in Fig. 5c. The hardness increase is maintained after the electrochemical treatment and therefore these processing steps represent a route through which

mechanically robust micro-textured surfaces could be generated which are closely related to the underlying material microstructure. This combination of microstructural modification and related EJM texturing is not possible using either laser processing methods, or electrochemical methods alone. The apparent inverse relationship between hardness and laser energy transferred, especially in the highest energy trials, is likely to be a result of both the observable decarburisation upon laser treatment and also coarsening of the prior austenitic grain structure caused by the slower cooling rates which are detailed in Fig. 2. The coarsening of the prior austenitic microstructure with input laser energy may lead to increases in the plate-thickness of the resulting martensite leading to the higher observable surface roughness.

Through EDS and Raman observations of the machined surfaces, it has been established that surface oxide phases present also provide a significant contribution to surface roughness increases, especially at higher energy pre-treatments above 1000 J. The apparent increase in surface oxide concentration only occurs as a consequence of higher energy pre-treatments, specifically when the material is heated beyond its melting point (1540 °C). It follows that the mechanism of oxide formation at the base of electrochemically machined tracks is at least partially dependent on pre-treatment associated thermal phenomena. It is proposed that the significant increase in oxygen signal observed at the EJM tracks at higher pre-treatment energies occurs partially as a result of increased oxygen diffusion throughout the melt-pool, in the pre-treatment step. A higher oxygen concentration within the material bulk after pre-treatment would likely lead to higher levels of accessible oxygen within the pre-treated material resulting in greater oxide formation during EJM.

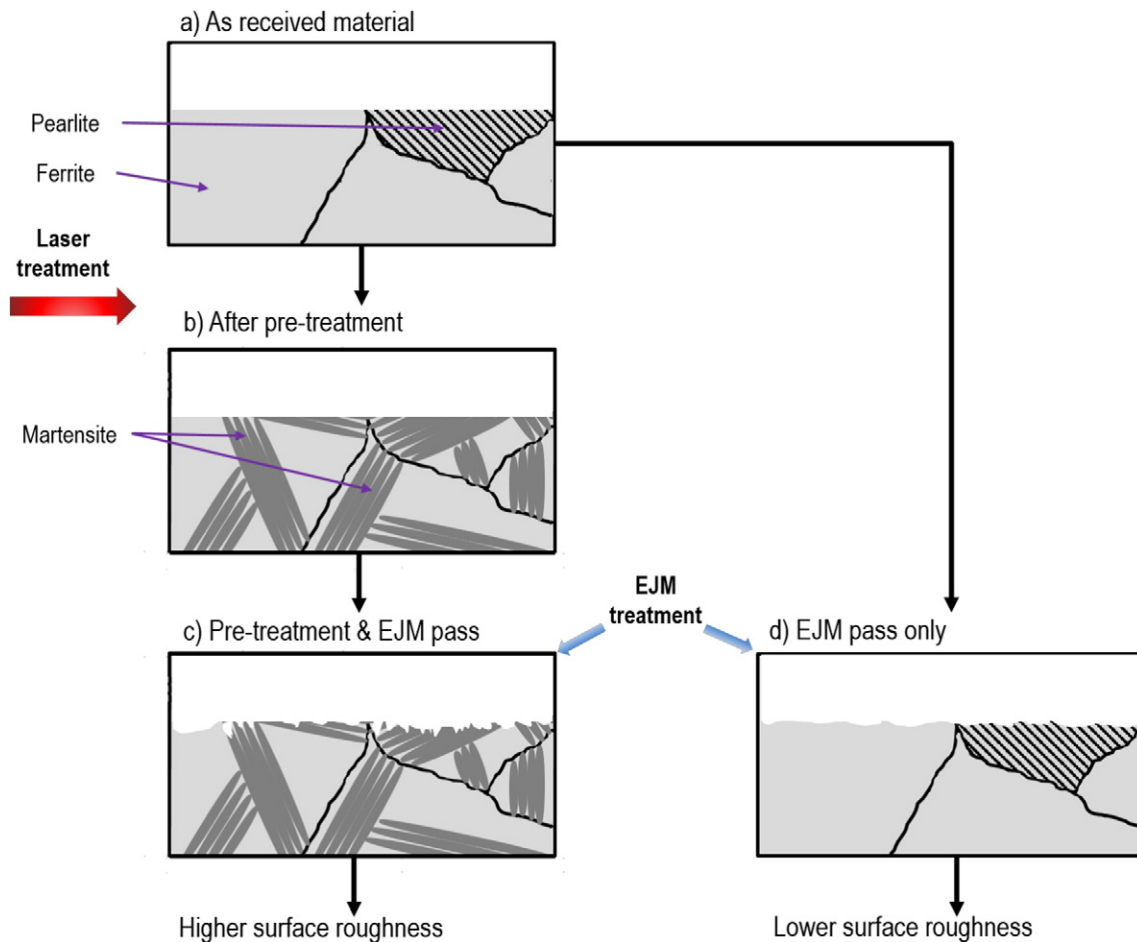


Fig. 10. a) As received material, b) martensite formation after laser pre-treatment, c) martensite exposure and increased roughness, d) EJM of untreated region and lower surface roughness.

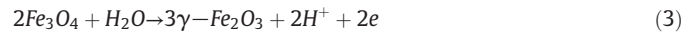
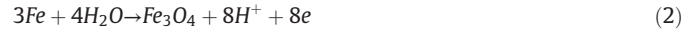
4.2. Surface and subsurface chemistry

4.2.1. Characterisation of surface oxides

On this basis the contribution of iron oxide species to the resulting machined surface textures cannot be ignored. During the Raman spectroscopic study of the EJM tracks, three phases of iron oxide have been observed and the particular occurrence of each species appears to be dependent on the current density of the machining process. Raman line-maps were acquired across the machined tracks in order to determine the localised distribution of two of the three common oxides: haematite, α - Fe_2O_3 and magnetite, Fe_3O_4 observed in this study. In this study it was not possible to assign vibrational modes to maghemite due to the band overlap and masking with haematite. The line maps were generated using the intensity of bands corresponding to expected haematite A_{1g} and E_{2g} stretching vibrations ($180\text{--}330\text{ cm}^{-1}$), and expected magnetite A_{1g} stretching vibrations ($600\text{--}750\text{ cm}^{-1}$) previously discussed in Section 2.3. High intensities correspond to high levels of each respective oxide and low intensities correspond to low levels of each particular oxide, or that the sample was out of focus at the acquisition point. The line-maps are given in Fig. 11 and appear to show the oxide chemistry of the track bases is dominated by haematite with very little magnetite, however translation to the extreme edges of the track resulted in a corresponding increase in magnetite and decrease in haematite. This effect appears occur independently of the laser treatment within the parameters of this study, which implies that this oxide transition is a result of the EJM process. Fig. 11 shows a schematic of the current density distribution curve of the process and the line-maps that correspond to the haematite-rich track base where the current density of the EJM process is very high, and the magnetite-rich track edges

where the current density of the EJM process is greatly reduced. It should be noted that where the haematite intensity appears to reduce in the right-hand region of the track base line-map and the left-hand region of the track edge line-map, the sample piece was not wholly in focus due to the shallow depth of field caused by the constraining geometry of the EJM track.

The anodic oxidation of iron has been shown to be a process where two discrete films form as part of the dissolution process [27]. The inner oxidation film has been shown to comprise at least partially, of magnetite, Fe_3O_4 , proposed to form as a result of Eq. (2). The magnetite then undergoes further oxidation to form a surface film of maghemite, γ - Fe_2O_3 , following Eq. (3), before further oxidation and removal into the waste electrolyte. Eq. (3) is reported to occur when the anodic potential is intensified [28].



Intuitively it follows that the areas where the highest levels of magnetite are observed are located where the EJM process has not been able to fully overcome the critical passivation potential of the iron and as a consequence, there is less observable Fe_2O_3 at the track edges. These regions of lower potential occur in zones of current density depletion within the jet.

Although not observed in this study, the presence of iron hydroxides as further oxidation products at the EJM processed surface cannot be excluded as in most cases they have been shown to transform to oxides of higher stability at low Raman laser power [30], therefore the lack of

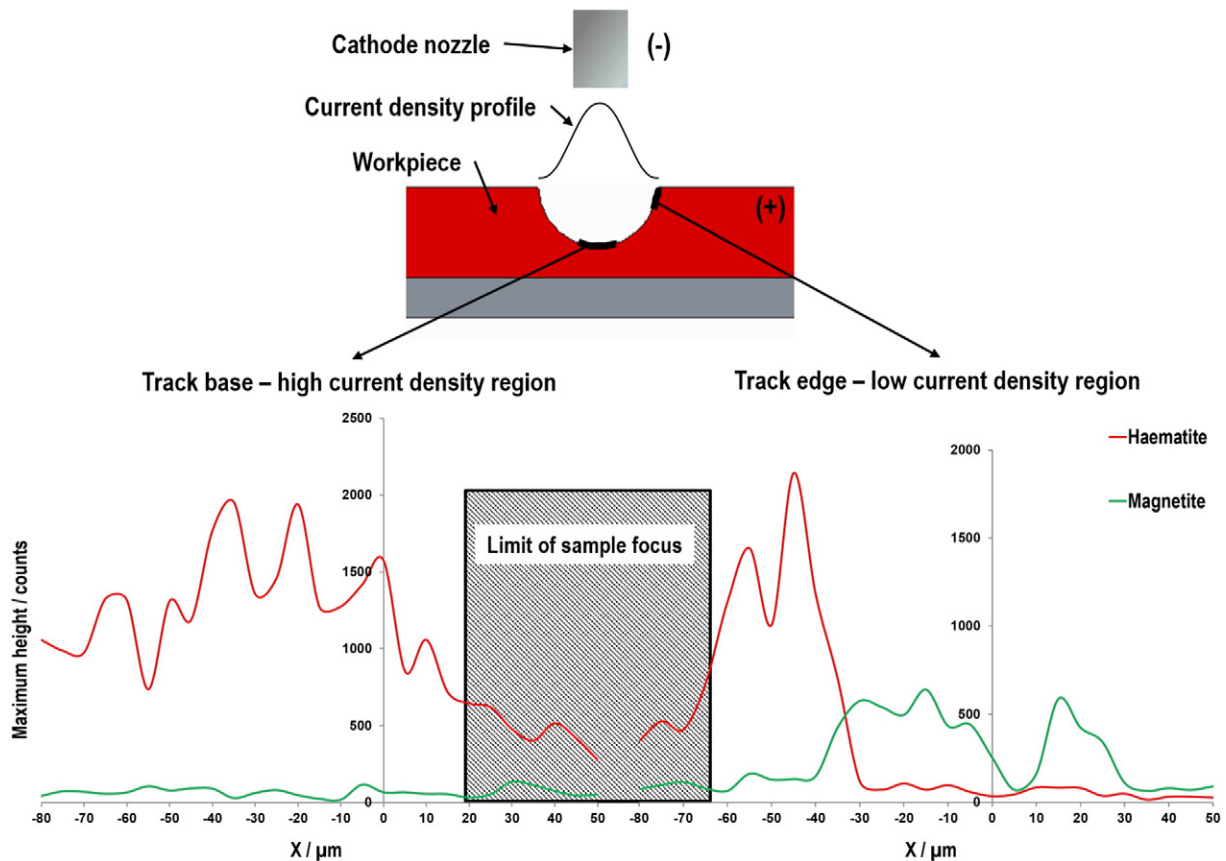


Fig. 11. Relating apparent surface oxide composition to incident current density during EJM; top) schematic showing current density distribution curve of the EJM process and line-map extraction areas, left) corresponding Raman spectroscopic line-map for track base, right) corresponding Raman spectroscopic line-map for track edge.

evidence for their existence may be an artefact of the technique. It should be noted that the positions all bands in this Raman spectroscopic analysis were slightly shifted to lower energies which could be a result of localised heating caused by high laser powers used in the Raman spectroscopic analysis. This would broaden and downshift the Fe—O stretching vibrations [26]. Lattice vibration energy is sensitive to grain size, therefore the downshifting of bands could also be an indicator of small grain sizes of the iron oxide phases analysed in this study [31].

4.2.2. Surface and near-surface carbon

In this study, the current density distribution across the EJM tracks has been shown to affect the chemistry of the surface oxide phases present. Carbon is also known to be a major surface-film former during the ECM of steels, in the form of iron carbides resulting from the higher electrical conductivity and therefore preferential machining of the α -Fe ferrite phase [32]. Preferential machining of metallic phases over carbides has previously been reported in EJM techniques for other material systems such as WC alloys [33,34]. In order to qualitatively appraise the effect of the current density distribution on surface carbon levels across the EJM track, the samples were cross-sectioned and EDS spectra were recorded at pre-set distances away from the surface in order to ascertain the depth of the carbon dominated films in relation to the current density. Fig. 12 shows the resulting composition gradients for iron and carbon at set depths from the observed track surface. There is a clear difference in the two carbon depletion gradients which appears to be significantly shallower at the base of the EJM track compared with the

side walls. This observation correlates well with the Gaussian current density distribution curve which has been directly observed within this study to influence the chemistry of the surface oxides. Material removal occurs at a slower rate at the track sides due to the low localised current densities. Intuitively residual carbon concentration at the EJM track is at least partially a function of the volume of material removed above the subsequent surface during the machining process. Material is removed at a slower rate at the track sides leading to a much slower rate of residual carbon accumulation in these areas. In the case of the track bases where the current density is high, material is removed at a much higher rate and therefore carbon accumulation is greater in these areas. It is proposed that this effect is responsible for the apparent steeper carbon gradient away from the surface in the lower current density regions such as the track sides. This effect is likely to be complemented by ‘wash-out’ in which electrochemically resistant phases for example iron carbides are removed by the washing effect of the impinging jet and not by anodic dissolution. For areas where the rate of material removal is low such as track sides, the carbon-rich surface will be exposed to these effects for significantly longer than areas where the material removal and the rate of carbon accumulation are greater.

The disparity between surface carbon in the pre-treated and untreated areas of the EJM track, supported by EDS and Raman spectroscopy, can be explained by metallurgical effects induced by the laser. Decarburisation is a well-reported phenomenon understood to occur when steels are heated beyond 700 °C, especially within an oxygen-

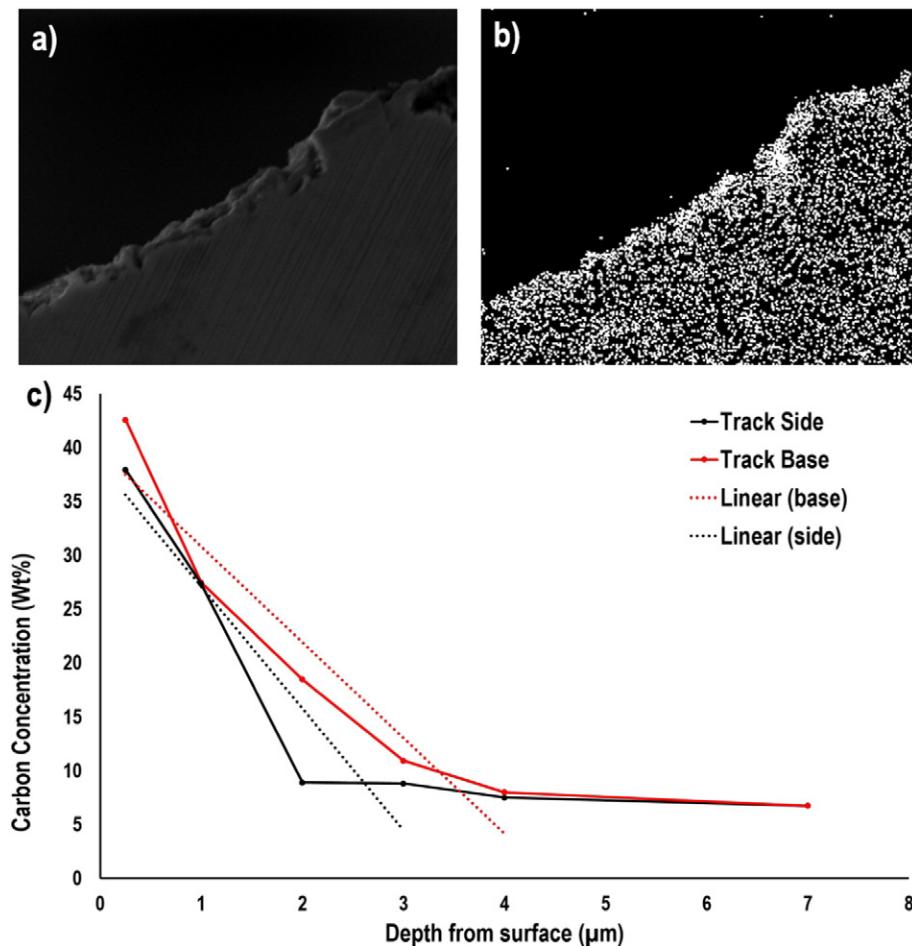


Fig. 12. a) Sectioned EJM track, b) surface carbon accumulation in elemental EDS map, c) graph showing carbon gradients at high current density (basal) areas (red) and low current density (side) areas (black).

rich atmosphere [23]. This decarburisation effect is likely to be complemented by effects relating to the microstructural changes that have occurred within the material during pre-treatment. Upon laser treatment, carbon is dissolved within the melt pool and upon recrystallization is contained as a solid-solution within the austenite phase. The subsequent diffusionless transformation from austenite to martensite prevents the time-dependent formation of the separated carbide phases. Carbide phases are known to be highly resistant to anodic dissolution, however when the carbon is trapped as an interstitial element within martensite or retained austenite, the decrease in phase conductivity would therefore be much lower. In the subsequent EJM process, carbon would then be removed with greater uniformity and fewer carbides would accumulate at the surface. This effect is proposed to complement the decarburisation phenomenon leading to greater depletion of carbon in the laser pre-treated areas.

4.3. Process window definition

In this study, pre-treatments where the total energy passed was <760 J were shown to have negligible effect on the measured roughness (S_a) after EJM treatment. It should also be noted that laser treatments of greater energy passed than 2000 J resulted in erratic EJM response, characterised by significant arcing over the electrodes during the nozzle traverse over the centre of the laser treated zone. The erratic response of the EJM treatment is largely considered to be a result of waviness of the laser treated surface. The stand-off distance between the nozzle and the workpiece, set to 500 μm in this work, is not dynamic leading to much smaller working gaps and short-circuiting in extreme cases where the laser pre-treatment creates large undulations in topography. In any case, the greatest energy pre-treatment studied here lead to both cracking and vaporisation of the material, shown in Fig. 13 (inset c), which is undesirable. The developed process window is shown in Fig. 13.

5. Conclusions

As a result of the models and processes presented here a new technique has been demonstrated for coupling of laser and electrolyte jet processes for the preparation of complex surfaces. For the first time EJM of laser pre-treated surfaces has been carried out on ferritic mild steel. As such a process window has been designed wherein the effect of laser treatment on the EJM response (roughness, S_a) of the material, in this case 39NiCrMo3, is optimised. It is proposed that the results from this preliminary experimental will expedite the use of this process in other material systems. Hardness has been demonstrated to increase after laser pre-treatment from approximately 261 HV to over 700 HV, and this hardness is shown to be retained after electrochemical treatment, an effect which is not possible when using EJM methods alone.

The roughness (S_a) of the EJM treated surface has been shown to increase from approximately 0.45–18 μm across a range of laser pre-treatments in a controllable fashion. The increase in the surface roughness has been shown to be partially a result of the laser-induced martensitic transformation that has been predicted, *via* simulation, and observed directly through optical and electron microscopic techniques. The martensite that has been shown to form in the laser treatment which is partially exposed by the electrochemical treatment leading to a rougher surface with plate type features present. The generation of surface textures that are as closely related to the underlying material microstructure is not achievable through other methods such as pulsed-laser processing. A further contribution to the increased surface roughness is demonstrated to arise from higher levels of oxide on the laser pre-treated surface, especially at higher energy pre-treatments, likely a diffusion phenomenon.

The chemistry of the surfaces and near subsurface of EJM machined tracks has been explored. This study found lower levels of surface carbon on electrochemically machined surfaces that had undergone laser pre-treatment to untreated machined surfaces. The difference has

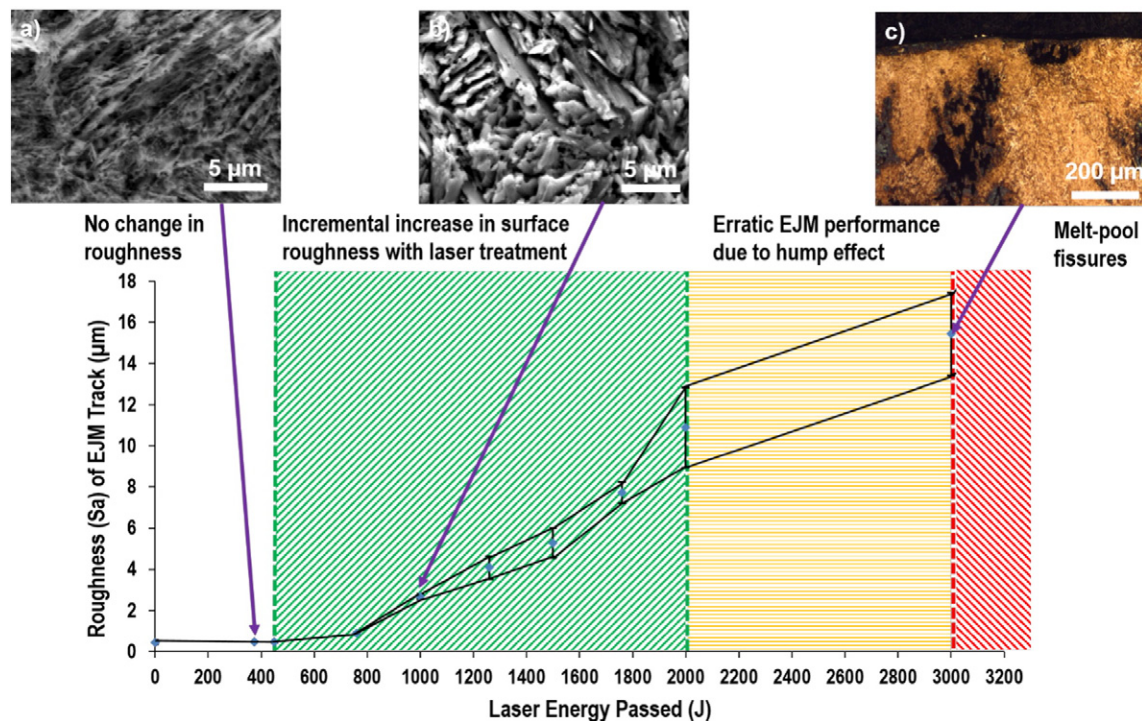


Fig. 13. Process window where effect of laser treatment on EJM performance is optimised (green area), inset a: No change in roughness with laser treatment in 375 J, inset b: incremental increase in surface roughness with pre-treatment energy of 1000 J, inset c: the void space, cracking and convex surface of the material where the energy passed was 3000 J.

been attributed to both decarburisation during the pre-treatment process as well as the laser-induced microstructural changes resulting in the distribution of carbon as an interstitial element within the martensite phase, and not the electrochemically resistant carbide phases. The gradient of carbon concentration away from the surface have here been observed using EDS of sectioned samples. Regions where the current density is lower, the gradient of carbon depletion with depth is greater. Also dependent on the localised current density, the chemistry of the iron oxide films is shown to change from haematite and maghemite, α and γ Fe_2O_3 respectively, at the high current density track bases, to higher concentrations of magnetite, Fe_3O_4 , at the track edges. It has been proposed that the reduced current density in the rim areas leads to the lower oxidation levels of the iron at the surface.

Acknowledgements

This work was supported by the Engineering and Physical Sciences Research Council (EPSRC) through EPSRC Centre for Doctoral Training in Innovative Metal Processing [grant number EP/L016206/1], and through In-Jet Interferometry for Ultra Precise Electrolyte Jet Machining [project EP/M02072X/1]. The authors would also like to thank Mr. Alexander Jackson-Crisp of ACEL, University of Nottingham.

References

- J.F. Wilson, *Practice and Theory of Electrochemical Machining*, Wiley-Interscience, New York, 1971.
- W. Natsu, T. Ikeda, M. Kunieda, Generating complicated surface with electrolyte jet machining, *Precis. Eng.* 31 (1) (2007) 33–39.
- M. H.-Oschätzchen, A. Martin, G. Meichsner, M. Kowalick, H. Zeidler, A. Schubert, Inverse jet electrochemical machining for functional edge shaping of micro bores, *Procedia CIRP* 6 (2013) 378–383.
- T. Kawanaka, S. Kato, M. Kunieda, J.W. Murray, A.T. Clare, Selective surface texturing using electrolyte jet machining, *Procedia CIRP* 13 (2014) 345–349.
- A. Speidel, J. Mitchell-Smith, D.A. Walsh, M. Hirsch, A.T. Clare, Electrolyte jet machining of titanium alloys using novel electrolyte solutions, *Procedia CIRP* 42 (2016) 367–372.
- M. H.-Oschätzchen, G. Meichsner, A. Schubert, Simulation of the shape of micro geometries generated with jet electrochemical machining COMSOL Conference, 2008 Hannover.
- T. Ikeda, W. Natsu, M. Kunieda, Electrolyte jet machining using multiple nozzles, *International journal of electrical machining* 11 (2006) 25–32.
- W. Natsu, S. Ooshiro, M. Kunieda, Research on generation of three-dimensional surface with micro-electrolyte jet machining, *CIRP J. Manuf. Sci. Technol.* 1 (1) (2008) 27–34.
- M. H.-Oschätzchen, G. Meichsner, A. Schubert, Generating micro geometries with air assisted electrochemical machining EUSPEN 10th International Conference 2008, pp. 420–424 Zurich.
- S. Skvarenina, Y.C. Shin, Predictive modeling and experimental results for laser hardening of AISI 1536 steel with complex geometric features by a high power diode laser, *Surf. Coat. Technol.* 201 (6) (2006) 2256–2269.
- M.A.S. Torres, H.J.C. Voorwald, An evaluation of shot peening, residual stress and stress relaxation on the fatigue life of AISI 4340 steel, *Int. J. Fatigue* 24 (8) (2002) 877–886.
- A. Fortunato, A. Ascari, E. Liverani, L. Orazi, G. Cuccolini, A comprehensive model for laser hardening of carbon steels, *J. Manuf. Sci. Eng.* 135 (6) (2013) 061002–061002.
- R.S. Lakkhar, Y.C. Shin, M.J.M. Krane, Predictive modeling of multi-track laser hardening of AISI 4140 steel, *Mater. Sci. Eng. A* 480 (1–2) (2008) 209–217.
- Y.S. Yang, S.J. Na, A study on residual stresses in laser surface hardening of a medium carbon steel, *Surf. Coat. Technol.* 38 (3) (1989) 311–324.
- W. Perrie, M. Gill, G. Robinson, P. Fox, W. O'Neill, Femtosecond laser micro-structuring of aluminium under helium, *Appl. Surf. Sci.* 230 (1–4) (2004) 50–59.
- K.M.T. Ahmmed, E.J.Y. Ling, P. Servio, A.M. Kietzig, Introducing a new optimization tool for femtosecond laser-induced surface texturing on titanium, stainless steel, aluminum and copper, *Opt. Laser. Eng.* 66 (2015) 258–268.
- U.A. Theilade, H.N. Hansen, Surface microstructure replication in injection molding, *Int. J. Adv. Manuf. Tech.* 33 (1) (2007) 157–166.
- X. Yang, X. Liu, Y. Lu, S. Zhou, M. Gao, J. Song, W. Xu, Controlling the adhesion of superhydrophobic surfaces using electrolyte jet machining techniques, *Sci. Rep.* 6 (2016) 23985.
- E. Liverani, A.H.A. Lutey, A. Ascari, A. Fortunato, L. Tomesani, A complete residual stress model for laser surface hardening of complex medium carbon steel components, *Surf. Coat. Technol.* 302 (2016) 100–106.
- A. Fortunato, L. Orazi, G. Tani, A new computationally efficient model for tempering in multitrack laser hardening in medium carbon steels, *J. Manuf. Sci. Eng.* 133 (2) (2011) 021003.
- J. Mitchell-Smith, A.T. Clare, J.W. Murray, Electrolyte Jet Machining for Surface Texturing of Inconel 718, *International Symposium on Electrochemical Machining Technology 2014*, pp. 111–118 Saarbrücken.
- J.A. McGeough, *Advanced Methods of Machining*, Chapman and Hall Ltd., UK, 1988.
- H.D. Alvarenga, T.V.D. Putte, N.V. Steenberge, J. Sietsma, H. Terry, Influence of carbide morphology and microstructure on the kinetics of superficial decarburization of C-Mn steels, *Metall. Mater. Trans. A* 46 (1) (2015) 123–133.
- I. Chourpa, L. Douziech-Eyrolles, L. Ngaboni-Okassa, J.F. Fouqueunet, S. Cohen-Jonathan, M. Souce, H. Marchais, P. Dubois, Molecular composition of iron oxide nanoparticles, precursors for magnetic drug targeting, as characterized by confocal Raman microspectroscopy, *Analyst* 130 (10) (2005) 1395–1403.
- A.M. Jubb, H.C. Allen, Vibrational spectroscopic characterization of hematite, maghemite, and magnetite thin films produced by vapor deposition, *ACS Appl. Mater. Interfaces* 2 (10) (2010) 2804–2812.
- D.L.A. Faria, S. Venâncio-Silva, M.T. Oliveira, Raman microspectroscopy of some iron oxides and oxyhydroxides, *J. Raman Spectrosc.* 28 (11) (1997) 873–878.
- C.L. Foley, J. Kruger, C.J. Bechtoldt, Electron diffraction studies of active, passive, and Transpassive oxide films formed on iron, *J. Electrochem. Soc.* 114 (10) (1967) 994–1001.
- M.I. Nagayama, M. Cohen, The anodic oxidation of iron in a neutral solution: I. The nature and composition of the passive film, *J. Electrochem. Soc.* 109 (9) (1962) 781–790.
- M.S. Dresselhaus, A. Jorio, M. Hofmann, G. Dresselhaus, R. Saito, Perspectives on carbon nanotubes and graphene Raman spectroscopy, *Nano Lett.* 10 (3) (2010) 751–758.
- M. Hanesch, Raman spectroscopy of iron oxides and (oxy)hydroxides at low laser power and possible applications in environmental magnetic studies, *Geophys. J. Int.* 177 (3) (2009) 941–948.
- I.V. Chernyshova, M.F. Hochella Jr., A.S. Madden, Size-dependent structural transformations of hematite nanoparticles. 1. Phase transition, *Phys. Chem. Chem. Phys.* 9 (14) (2007) 1736–1750.
- L.J.E. Hofer, E.M. Cohn, Some reactions in the iron-carbon system - application to the tempering of martensite, *Nature* 167 (4259) (1951) 977–978.
- M. H.-Oschätzchen, A. Martin, G. Meichsner, M. Zinecker, A. Schubert, Microstructuring of carbide metals applying jet electrochemical machining, *Precis. Eng.* 37 (3) (2013) 621–634.
- K. Mizugai, N. Shibuya, M. Kunieda, Study on Electrolyte Jet Machining of Cemented Carbide 37th International MATADOR Conference 2012, pp. 83–86 Manchester.